Supplementary text

Manuscript title:
Efficient, Polarization-diverse State Generation with Tunable Black Phosphorus Cavity Heterostructures and Active Metasurfaces

Authors:
Samuel K.W. Seah, Souvik Biswas, Claudio U. Hail, Min Seok Jang, Harry A. Atwater

Number of supplementary pages:
8

Number of supplementary figures:
8

S1. Design considerations for BP devices

The typical refractive index profile for sufficiently thin BP (below the Thomas-Femi screening length of 2-3nm for charge densities accessed in this work) is dominated by the exciton absorption. The Lorentzian lineshape for 3L-BP is given as an example in Fig. S1A. When gated, the oscillator strength of the exciton decreases in magnitude due to increased screening from the induced free carriers. Notably, the tail end of the real part of the refractive index at higher wavelengths decays noticeably slower compared to its imaginary counterpart (Fig. S1B).

This forms the basis for incorporating BP with exciton resonances detuned significantly below the operating wavelength. Because the refractive index change effected during gating (Δn) decays slower than loss k (Fig. S1C), it is possible to reduce overall excitonic losses while maintaining sufficient phase pickup. Maximizing the $\Delta n/k$ metric helps in this respect. The upper bound for wavelength detuning is governed by free electron absorption at higher wavelengths, and also the maximum Q that a DBR cavity can reasonably achieve, since the overall reduction in Δn must then be compensated by use of a high-Q cavity to ensure that the phase pickup is still sufficiently high. Given the vast applications of polarization control in the telecommunications wavelength, we chose the C-band as our operating wavelength while still maintaining a $\Delta n/k$ of 40.

For the devices incorporating graphene presented in Fig. 3 & 4, we make a direct comparison of material related losses in Fig. S1D. Here, loss is defined as absorptive loss for a single pass in the case of BP and graphene, and as the fraction of non-reflected power in the case of 300nm thick gold and an 18-pair TiO_2/SiO_2 DBR back reflector. The significant advantage of using non-lossy DBRs compared to gold is apparent. Furthermore, when graphene is introduced into the cavity, it dominates overall loss compared to 1-2L BP. This motivates the change in switching to 3L-BP for graphene incorporated devices, since the exciton resonance for 3L-BP is much closer to the C-band, allowing stronger exciton interactions within these relatively low Q devices.

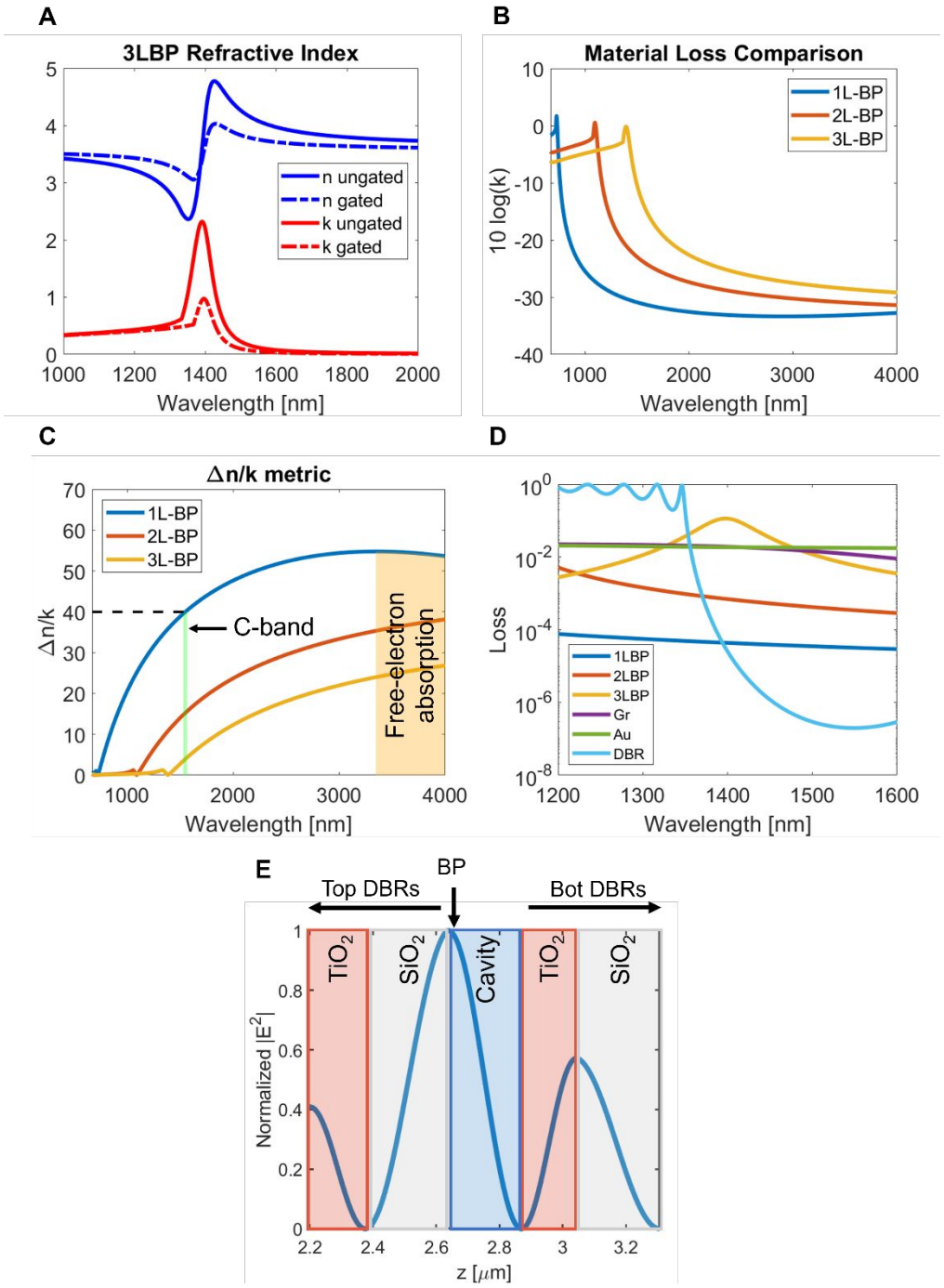

Fig S1. Design considerations for high efficiency anisotropic phase and amplitude modulation devices. (**A**) Modelled values for the real and imaginary parts of the refractive index for 3L-BP, as a function of gating. The Lorentzian lineshape from the excitonic absorption at 1398nm, continuum absorption at lower wavelengths, and relatively slow decay of n at higher wavelengths are all observable here. (**B**) Imaginary component of refractive index for monolayer and trilayer BP. (**C**) Phase modulation metric plot for monolayer BP. Refractive index change effected during gating (Δn) ideally must be maximized per unit loss (k) through the material. The C-band, as well as the wavelength ranges where free-electron absorption is significant, is highlighted. (**D**) Sources of loss for BP modulation devices. Loss is defined as the absorptive loss for a single pass through a 2D material, or as (1 – Reflected Power) in the case for 300nm Au and an 18-pair TiO_2/SiO_2 DBR mirrors. (**E**) Normalized electric field intensity as a function of

stack height for the amplitude modulation device in Fig. 1D, showing electric field maximum at the top of the central cavity where the active tuning material is placed.

Other design considerations not mentioned in the main text also include:

1. **Placement of BP near the top of the cavity**. This was done in order to maximize the interaction between the incident electric field and BP, since the electric field is maximum at the top of the cavity (Fig. S1E).
2. **Free carrier tunnelling through hBN**. Each hBN spacer layer separating any two 2D layer is kept to be minimally 2nm, since this ensures that the interlayer tunnelling resistance exceeds 10^{11} Ω μm² [1]
3. **Achieving critical coupling**. The number of DBR top layers act as an output coupler that controls the average number of roundtrips within the cavity. After choosing the number of top layers, the bottom hBN thickness is adjusted to attain a cavity resonance that is around the C-band. The thickness is then further fine-tuned towards or away from the exciton resonance as a means of adjusting the intra-cavity loss in order to achieve the critical coupling condition. The overall Q of the DBR cavity is restricted to a maximum of 11000, in line with current state-of-the-art DBR fabrication schemes. Furthermore, the device designs are found to be robust to bottom hBN layer thickness fluctuations (discussed in section S10).
4. **Doping density limitations**. The upper and lower bounds of the BP carrier density is restricted primarily by the dielectric breakdown of hBN. Data for this was derived from ref [2], and the corresponding charge density calculated using a capacitance model to be between 10^{11} and 10^{13} cm^{-2}.

S2. Gating trajectories for anisotropic phase and amplitude modulation device

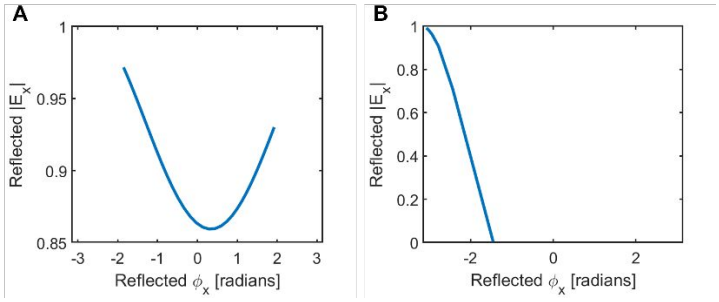

Fig S2. Amplitude and phase trajectories as a function of gating voltage for the (**A**) Phase modulation device (Fig. 1A). (**B**) Amplitude modulation device (Fig. 1D)

S3. Using input polarization angle and input wavelength as control parameters

For the anisotropic phase modulation device, tuning the input polarization angle shifts the voltage trajectory along the S_1 axis of the Poincare sphere (Fig. S3A). This can be understood by considering that the input polarization states rotate around the equator of the Poincare sphere as the polarization angle increases. For an input polarization angle between 0 and 90 degrees, 60% of the Poincare sphere surface is covered, while for an input polarization angle range between 0 and 180 degrees, all polarization states on the Poincare sphere can be accessed.

Changing the input wavelength on the other hand rotates the voltage trajectory along the S_2/S_3 plane (Fig. S3B). This occurs because as the operating wavelength shifts away from the critical coupling condition, the phase shift between the x and y components of the incident light decreases. The total tunable phase range also decreases, causing the trajectory to shrink.

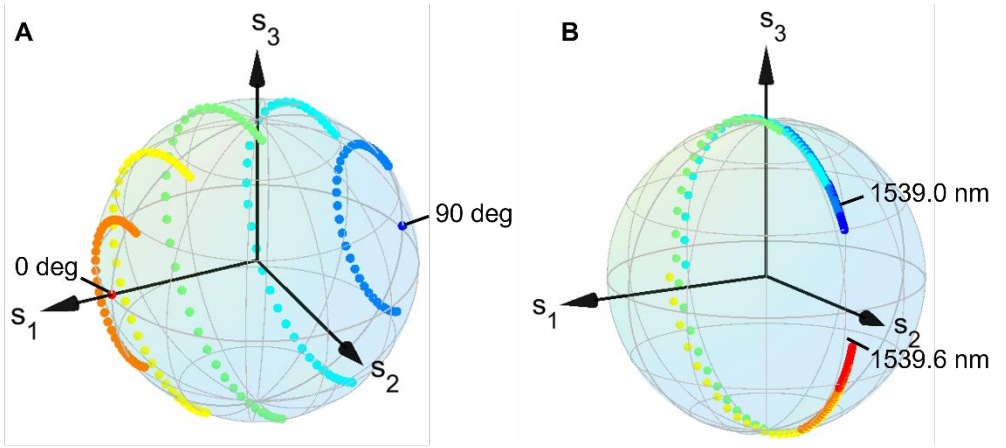

Fig S3. Additional Poincare sphere voltage trajectory plots for the phase modulation device shown in Fig. 1A as a function of: (**A**) Input linear polarization angle, ranging from 0 to 90 degrees (in increments of 15 degrees), with input wavelength kept at 1539.3nm. (**B**) Input wavelength, in increments of 0.1nm, with input polarization angle kept at 43°. Critical coupling occurs at 1539.3nm (green plot, same as Fig. 2A).

S4. Graphene conductivity and refractive index plots

The intraband and interband contributions to overall graphene conductivity are plotted here for comparison (Fig. S4). A moderate p-doping value of -0.4eV is used to shift the interband transition towards shorter wavelengths, thereby minimizing the optical loss due to both interband and intraband absorption within the operating wavelength for all gating voltages considered.

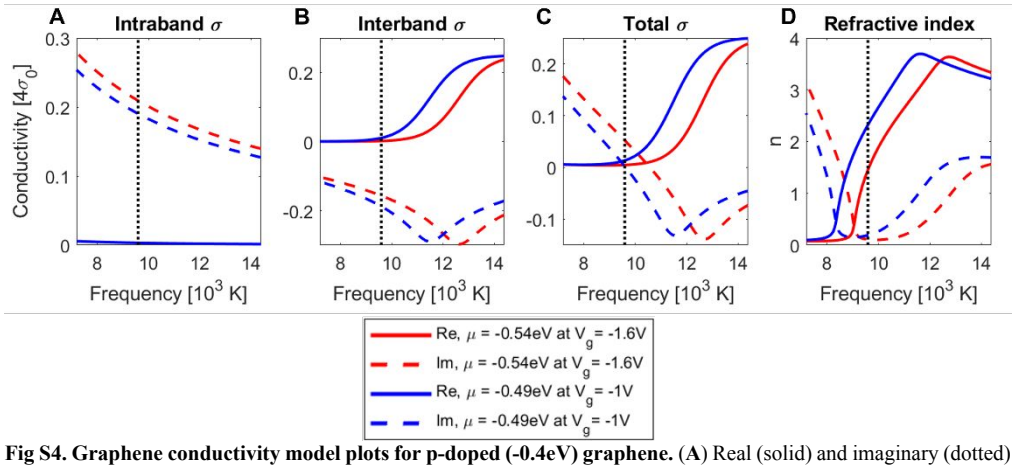

Fig S4. Graphene conductivity model plots for p-doped (-0.4eV) graphene. (**A**) Real (solid) and imaginary (dotted) intraband contributions to optical conductivity in units of $e^2/\hbar$ at high (red) and low (blue) doping concentrations. The dotted black line demarcates the operating frequency for the device in Fig. 4. (**B**) Interband contributions to optical conductivity. (**C**) Total conductivity of modelled graphene. (**D**) Calculated real and imaginary parts of refractive index. The graphene has been pre-doped such that when half-gated, the interband absorption is equal to the intraband absorption when maximally gated.

S5. Spectral reflected intensity and phase of 2 control parameter BP device

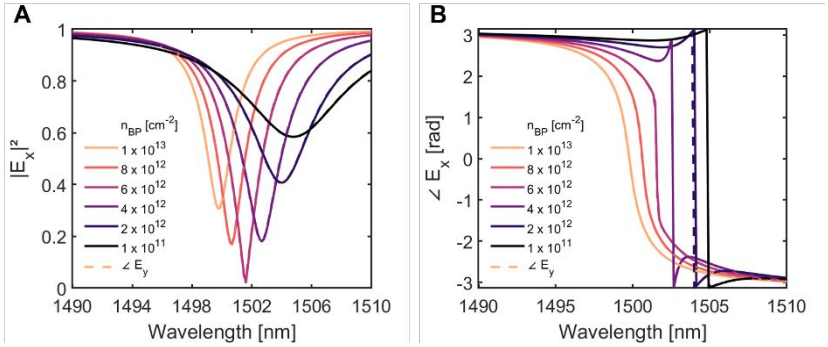

Fig S5. Intensity and phase plots as a function of doping densities for the (**A**) Electric field intensity plot corresponding to the 2 control parameter device shown in Fig. 3A. Solid lines represent the E_x field intensity, while dotted lines represent the E_y field intensities. The different colors represent different doping densities. (**B**) Phase modulation plot for the 2 control parameter device

S6. 2 control parameter polarization tuning device with no graphene contacts

While the device shown in Fig. 3 uses graphene contacts that can be further patterned to achieve a polarization beam splitting effect, we note that it is possible to make the device more efficient for the sole purpose of dynamic polarization conversion. This can be done by removing the graphene contacts. Since intracavity loss is no longer graphene-dominated, the BP can be detuned to 2 layers. This allows both phase and amplitude modulation to be simultaneously achieved, which is an important factor for covering different polarization states on the Poincare sphere. Increasing the number of top DBR pairs to 8 allows critical coupling to be achieved.

The device design and results are shown in Fig. S6. In this design, 95% of amplitude modulation and 282° of phase modulation along both the x and y directions can be achieved. With 45° linearly polarized light incident on the device, the output polarization states span >90% of the Poincare sphere surface.

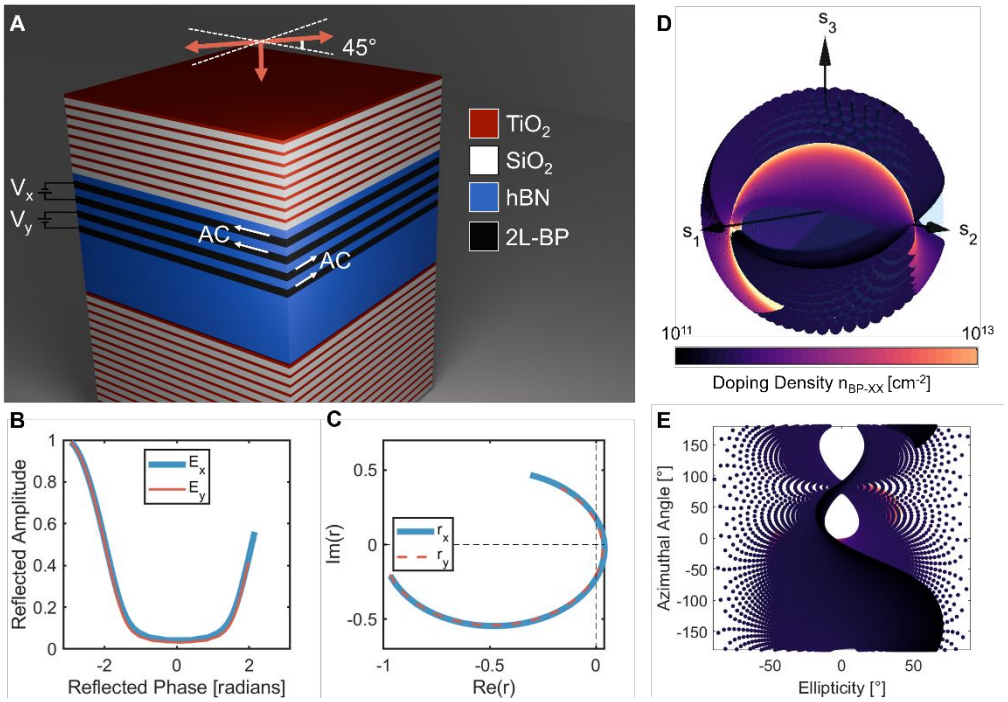

Fig. S6. Schematic of a BP device with two degrees of freedom, without lossy graphene contacts. (**A**) Illustration of the twisted-BP device. The top (bottom) two BP layers are aligned with its armchair (AC) axis parallel to the x-direction (y-direction). Mutual gating of the co-aligned BP layers pairwise gives independent control in both principal axes. 8 top TiO2/SiO2 DBR top pairs are required to achieve critical coupling. 3nm thick hBN spacer layers are employed between layers, with the bottom hBN spacer being 190nm. (**B**) Amplitude and phase for the x & y-components of reflected light as a function of gating voltage. (**C**) Complex reflectivity plot for the same data as in (B). (**D**) Normalized Poincare sphere coverage of device based on V_x and V_y tuning, with V_x tuning represented in color (black to peach). (**E**) Sampled polarization coverage of device as in (D), shown as a function of elliptical and azimuthal angles.

S7. Changing polarization beam splitting diffraction angle

FDTD simulations were performed for an 8-cell device where the repeat number of the sub-cells shown in Fig. 4B is 2 (Fig. S7). Far field projections performed calculated the diffraction angle at 5.4°, which is half of the angle show in Fig. 5C. The total device dimensions used for the far-field projection is 32 μm (along the patterning direction), by 32 μm (along the length of the ribbons). The polarization purity of the LCP/RCP light was found to be $|S_3| > 0.86$.

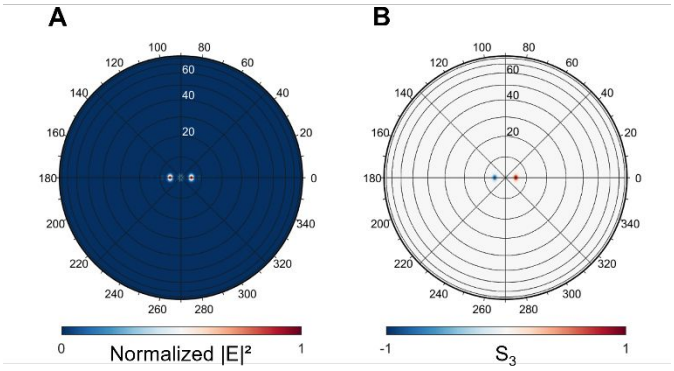

Fig S7. Hemispherical far-field projections for 8-cell device with a repeat number of 2. (**A**) Normalized electric field intensity output of 8-cell device. Each radial segment demarcates 10° angular separation. (**B**) Hemispherical far-field projection of S_3 parameter, showing polarization beam splitting at 5.4°.

S8. Additional functionalities of polarization beam splitting device

We note that while polarization beam splitting is possible with the device presented in Fig. 5, other functions can be performed by the device as well. For example, regular diffraction beam splitting conventionally achieved using isotropic materials can be emulated by gating the top and bottom layers with identical voltages, while creating an alternating voltage grating across the row of the device (Fig. S8A). Similarly, if LCP/RCP light is incident on the device, its handedness can be flipped by inducing a 180° phase shift between the x and y components. Beam splitting can then be added by inducing a 180° phase difference between adjacent subcells (Fig. S8B). These examples demonstrate the versatility of the device in achieving a variety of polarization control effects in conjunction with tunable diffraction beam splitting.

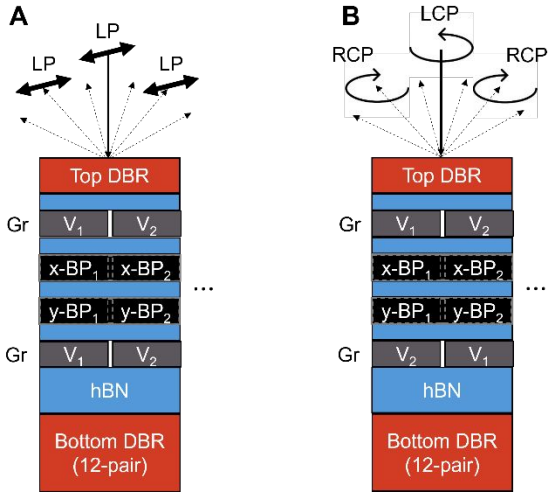

Fig. S8. Cross-section of the device supercell with gating configurations for (**A**) Diffraction beam splitting and (**B**) Beam splitting of circularly polarized light while flipping the handedness

S9. Broad bandwidth, lower Q design of phase modulator device

While the phase modulation device demonstrated in Fig. 1A achieves 210° of dynamic tuning range at high optical efficiencies exceeding 87%, we note that the operating bandwidth is relatively small due to the high-Q factor of the structure. An alternative structure is proposed here which incorporates 2L-BP (as in Fig. 1D), but with a 260nm-thick bottom hBN layer. This allows the device to operate in the undercoupled regime to maintain 210° of dynamic tuning range over a 0.5nm bandwidth, but at the cost of the optical efficiency dipping to 35-98% (Fig. S9). This is due to the lower cavity Q-factor of 5800.

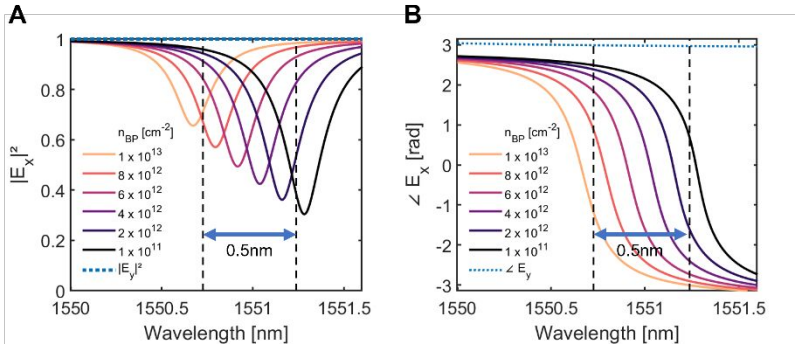

Fig. S9. Performance of an undercoupled, broadband 2L-BP device for phase modulation. (**A**) Amplitude fluctuates between 35% and 98% for this design. (**B**) A dynamic phase modulation range of 210° (indicated by the dotted black lines) is achieved over a 0.5nm bandwidth.

S10. Sensitivity of phase and amplitude modulator devices to bottom hBN thickness

While the 2D materials presented in Fig. 1 are of fixed thicknesses, such precise material thicknesses are difficult to achieve in fabrication. Here, modulation results for differing bottom hBN thicknesses are presented (Fig. S10). For the phase modulator device in Fig. 1A, changes in the hBN layer by ±5nm still result in >209° phase tuning range with 87-97% efficiency. For the amplitude modulator in Fig. 1D, a ±5nm difference in hBN thickness results in an 87-97% amplitude modulation range with a 1.5 radian phase modulation.

We note that for the amplitude modulator device, decreasing the bottom hBN thickness increases the overall loss in the device, but this can be compensated for by operating at a higher minimum carrier density, resulting in a smaller impact in amplitude modulation range. Conversely, increasing the hBN thickness results in undercoupling at all carrier densities up to the hBN breakdown limit, and it is this inability to achieve critical coupling that results in a steeper drop in amplitude modulation range.

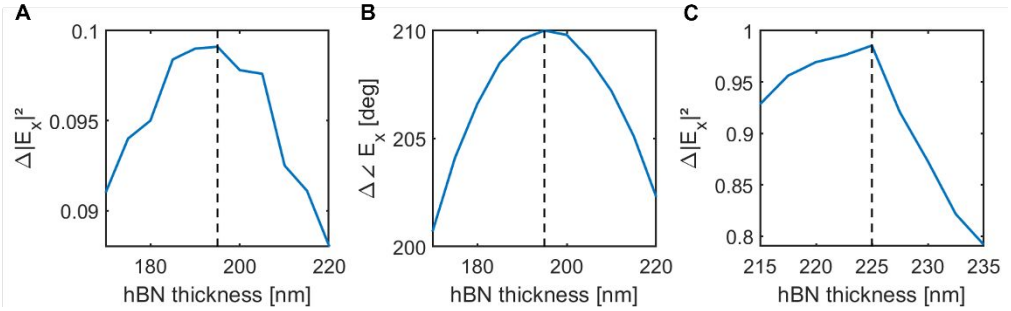

Fig. S10. (**A** and **B**) Amplitude and phase modulation ranges for the phase modulator device presented in Fig. 1A, as a function of bottom hBN thickness. The black dotted lines show the optimal hBN thickness of 195nm. (**C**) Amplitude modulation range for the amplitude modulator device presented in Fig. 1D, as a function of bottom hBN thickness. Here, the amplitude modulation range is taken at the wavelength where overall phase modulation is less than 1.5 radians. The black dotted lines show the optimal hBN thickness of 225nm.

S11. Amplitude modulation device with minimal phase fluctuation

The amplitude modulator device presented in Fig. 1D was optimized for optical efficiency rather than suppressing phase modulation. Here, we present a more conventional scheme focused on reducing unwanted phase fluctuations during amplitude modulation. For aggressive amplitude modulation, it is more desirable to use thicker 3L-BP, with gold mirrors instead of DBRs to maximize loss in the system per roundtrip (Fig. S11A). By operating at a wavelength slightly red-shifted from the critical coupling condition, 19 dB of amplitude tuning is achieved with only 0.2 radians of phase change (Fig. S11B, C). However, this approach is optically inefficient, with peak optical efficiencies reaching only 23%, as opposed to the 99% efficiencies shown in Fig. 1D.

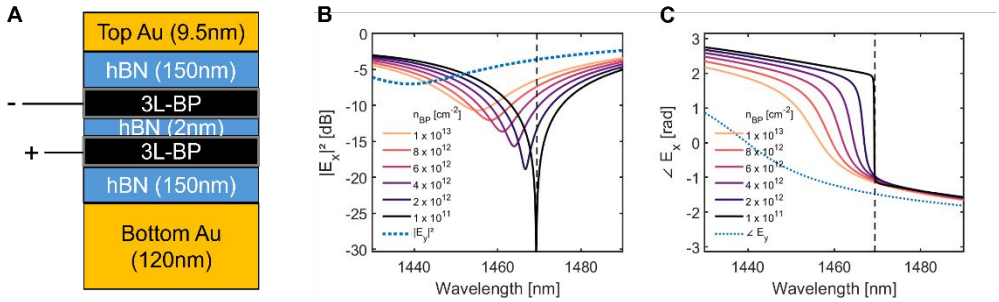

Fig. S11. Schematic for an amplitude modulation device using co-aligned 3L-BP and gold mirrors. (**A**) An amplitude modulation of up to 19dB is possible, with a peak optical efficiency of 23%. (**B**) Phase fluctuation of 0.2 radians occurs at the operating wavelength.

SUPPLEMENTARY REFERENCES

1. L. Britnell *et al*., *Nano Lett*. **12**(3), 1707-1710 (2012).
2. S. Biswas, M. Y. Grajower, K. Watanabe, T. Taniguchi, H. A. Atwater, *Science* **374**, 448-453 (2021).